Hydrodynamic CFD-DEM model validation in a gas-solid vortex unit

Florian Wéry[1]

Laurien A. Vandewalle[1], *Guy B. Marin*[1], *Geraldine J. Heynderickx*[1], *Kevin M. Van Geem*[1]*

[1]Ghent University, Laboratory for Chemical Technology, Technologiepark 125, 9052 Gent, Belgium.

*Corresponding author: Technologiepark 125, 9052 Gent, Belgium; Kevin.VanGeem@UGent.be

Abstract:

Process intensification in gas-solid fluidization processes can be achieved by working in a centrifugal rather than a gravitational field. In this regard, the gas-solid vortex unit (GSVU) is an ideal candidate for heterogeneously catalyzed processes. A four-way coupled CFD-DEM model describing the hydrodynamics in the GSVU with an unprecedented level of detail is validated using 2D particle image velocimetry (PIV) experimental data on both azimuthal and radial particle velocity components. It captures high and low velocity regions, both qualitatively and quantitatively. Gas-solid slip velocities several times higher than those obtainable in a gravitational field are achieved, greatly enhancing heat and mass transfer rates. Furthermore, the gas-phase residence time distribution in the GSVU is shown to be narrow. This developed model presents a powerful tool for a better understanding and a detailed design aimed at enhancing the non-reactive and reactive process intensification capabilities of the gas-solid vortex technology.

Keywords: process intensification, CFD-DEM, model validation, fluidization, vortex

1. INTRODUCTION

Nowadays, heterogeneously catalyzed processes are omni-present in the chemical industry. Fluidized bed reactor technology allows for efficient heat and mass transfer and convenient catalyst regeneration. A fluidized bed reactor (FBR) is used, amongst others, in fluid catalytic cracking [1], methanation [2], Fischer-Tropsch synthesis [3] and several polymerization processes [4-6]. FBRs are also used in physical processes including drying [7-9] and particle coating [10, 11]. Nevertheless, mass and heat transfer can still be improved, e.g. when operating in a bubbling flow regime observed at a fairly low gas inlet velocity. Gas bubbles can flow through the bed by-passing the solid particles. Upon increasing the gas inlet velocity, turbulent fluidization is observed, elongating the bubbles and increasing the gas-solid contact [12]. However, when the gas-solid slip velocity exceeds the terminal free falling velocity of the particles, particles are entrained with the gas-flow.

Gas-solid slip velocities can be increased without leading to particle entrainment by operating in a centrifugal rather than a gravitational force field. This is known to contribute to process intensification (PI), since it allows for larger flows to be handled in smaller and more energy-efficient reactors. Two categories of centrifugal FBRs can be distinguished. In a rotating unit, a so-called rotating fluidized bed (RFB), momentum is supplied to the solids via a rotating axis powered by a motor [13]. The rotational speed of the motor acts as an additional degree of freedom such that a stable bed can be achieved in a wide range of operating conditions. These RFBs show great potential in drying operations [14]. In a static unit, momentum is transferred to the solids by introducing the process gas via tangentially inclined inlet slots. Since the static geometry does not induce any mechanical vibrations, the latter option is inherently simpler and safer [15]. The static geometry is referred to as a RFB in a static geometry (RFB-SG) or a gas-solid vortex unit (GSVU)

[16]. A GSVU can potentially be used for reactive processes like fluid catalytic cracking [17], oxidative coupling of methane (OCM) [18], gas separation by adsorption [19] and biomass pyrolysis [20]. In view of process intensification, several other measures can be taken to improve interfacial heat and mass transfer in FBRs [21, 22]. In a gravitational FBR, the use of internals such as membranes and baffles or mechanical agitators such as impellers aid in redistributing the gas flow and disrupting bubble formation [23, 24]. Gas pulsation or the use of multiple gas injectors allows to obtain a dynamically structured bed to increase the local level of micro-mixing [22]. Furthermore, other PI techniques such as induction or microwave heating can be implemented to supply heat to the system [25, 26]. Next to supplying heat to the solid material, an external electromagnetic field can be used to create particle chains via dipole-dipole interactions and alter the fluidization characteristics, stabilizing bubbling beds [27]. Additional momentum could be transferred to the particles via mechanical vibration of the FBR [28].

In order to speed up the reactor design of intensified geometries, digital twins can be employed. When adequate numerical models are combined with a thorough validation study based on experimental data, these digital twins can be both more cost and time effective compared to an extensive experimental campaign. Two main approaches are used when it comes to gas-solid two-phase flow: Eulerian-Eulerian and Eulerian-Lagrangian modeling. In the former, the gas and solid phase are treated as interpenetrating fluids and the Navier-Stokes equations are solved for both phases. Solving the Navier-Stokes equations for the solid phase implies that fluid-like properties are attributed to the solid phase. In this regard, the kinetic theory for granular flow, derived from a Chapman-Enskog expansion [29], is used. A main advantage of Eulerian-Eulerian modeling is the fairly low computational cost, whereas a main disadvantage is the inability to describe some of the essential properties of the particulate phase such as its discrete character. Previous numerical studies of the GSVU predominantly opted for the Eulerian-Eulerian framework. Niyogi et al. and Vandewalle et al. both performed a hydrodynamic parameter study of the GSVU [18, 30]. The intensification potential of the GSVU for interfacial heat transfer was numerically investigated by de Broqueville et al. [31]. In Eulerian-Lagrangian models, the discrete character of the solid phase is retained by tracking the trajectories of individual particles or clusters of particles and explicitly accounting for collisions between particles or clusters. CFD-DEM is an Eulerian-Lagrangian approach that combines computational fluid dynamics (CFD) with the discrete element method (DEM) [32, 33]. This method is computationally more expensive than the Eulerian-Eulerian approach since each particle is tracked individually. However, as more high-performance computing facilities become available CFD-DEM becomes an interesting tool for the numerical study and design of production units involving gas-solid flow [34]. A study by Verma et al. opted for coarse-grained DEM models to investigate particle segregation in the GSVU [35]. The coarse-grained DEM method groups discrete particles into a parcel that is tracked in the unit [36, 37]. De Wilde et al. illustrated some of the advantages of the more detailed CFD-DEM modeling approach without including an experimental validation study in the centrifugal field [38].

In this work, for the first time, a CFD-DEM framework applicable in the GSVU is validated in the centrifugal field via 2D particle image velocimetry (PIV) measurements on radial and azimuthal particle velocity components. This study uses experimental data gathered by Quiroga et al. [39]. Following the validation study, the model is applied to investigate the GSVU flow field in regions inaccessible for PIV measurements. Additionally, the potential to conduct OCM or biomass pyrolysis in the GSVU is assessed based on its ability to intensify heat and mass transfer.

2. MODEL DESCRIPTION

2.1. GAS-PHASE GOVERNING EQUATIONS

All CFD-DEM simulation results discussed in this work are performed with an in-house modified version of the open-source code CFDEMcoupling [40]. The modified version of CFDEMcoupling couples the open-source CFD solver OpenFOAM-8 [41] with the DEM solver LIGGGHTS 3.8 [42]. Based on the classification of Zhou et al., a 'Model A' approach is adopted in this work [43]. The gas phase continuity equation is given by:

$$\frac{\partial \varepsilon_g \rho_g}{\partial t} + \vec{\nabla} \cdot \left(\varepsilon_g \rho_g \vec{u}_g \right) = 0 \tag{1}$$

with ε_g the gas-phase volume fraction.

The gas-phase momentum equation is given by:

$$\frac{\partial \varepsilon_g \rho_g \vec{u}_g}{\partial t} + \vec{\nabla} \cdot \left(\varepsilon_g \rho_g \vec{u}_g \vec{u}_g \right) + \mathrm{K}_{gs}\left(\vec{u}_g - \vec{u}_s \right) = \varepsilon_g \rho_g \vec{g} - \varepsilon_g \vec{\nabla} p + \vec{\nabla} \cdot \left(\varepsilon_g \bar{\bar{\tau}}_g \right) \tag{2}$$

where $\bar{\bar{\tau}}_g$ is the gas-phase stress tensor, given by:

$$\bar{\bar{\tau}}_g = \left(\mu_g + \mu_{g,t} \right) \left[\left(\vec{\nabla} \vec{u}_g + \vec{\nabla} \vec{u}_g^{\,T} \right) - \frac{2}{3} \left(\vec{\nabla} \cdot \vec{u}_g \right) \bar{\bar{I}} \right] \tag{3}$$

With $\mu_{g,t}$ the turbulent contribution to the dynamic viscosity μ_g, calculated using the shear stress transport (SST) k-ω turbulence model [44]. The SST k-ω turbulence model was found to be very suitable in swirling flow applications as observed in a GSVU [18, 45, 46]. Applying the SST k-ω model includes the use of the k-ω turbulence model in the viscous boundary layer near the chamber walls, while the k-ε turbulence model is applied in the freestream region. The contribution of each of both turbulence models to the SST k-ω model is calculated via a blending function.

K_{gs} represents the momentum exchange coefficient between the gas and solid phase calculated using:

$$K_{gs} = \frac{\left|\sum_{s=1}^{N} \vec{F}_{d,s}\right|}{\left|\vec{u}_g - \vec{u}_s\right| V_{cell}} \tag{4}$$

The momentum exchange coefficient comprises of a summation of the drag force, $\vec{F}_d$ acting on every particle s in the CFD cell. The pressure gradient force, $\vec{F}_p$, and viscous forces, $\vec{F}_\mu$, acting on the particles are accounted for in the second and third term of the right-hand side of Eq. (2) based on the 'Model A' formulation [43]. These are not included in the momentum exchange term, K_{gs}, but are accounted for in the solid governing equation. For the drag force, Gidaspow's correlation is employed, combining the Ergun equation [47] in regions where the solid phase volume fraction ε_s is equal or higher than 0.2, with the Wen and Yu equation [48] in regions where the solids volume fraction is lower than 0.2. The mathematical formulation of the forces is listed in Table 1.

Table 1: Gas-particle interaction forces.

Drag force	
$\vec{F}_d = \beta_{gs}(\vec{u}_g - \vec{u}_s)V_s$	
$\beta_{gs} = \frac{3}{4} C_d \frac{(1-\varepsilon_g)\rho_g\lvert\vec{u}_g - \vec{u}_s\rvert}{d_s} {\varepsilon_g}^{-2.65}$, with	$\varepsilon_s < 0.2$
$C_d = \frac{24}{Re_s}[1 + 0.15(Re_s)^{0.687}]$	$Re_s < 1000$
$C_d = 0.44$	$Re_s \geq 1000$
$\beta_{gs} = 150 \frac{(1-\varepsilon_g)\mu_g}{\varepsilon_g d_s^2} + 1.75 \frac{\rho_g\lvert\vec{u}_g - \vec{u}_s\rvert}{d_s}$	$\varepsilon_s \geq 0.2$
Pressure gradient force	
$\vec{F}_p = -V_s \vec{\nabla} \mathrm{p}$	
Viscous force	
$\vec{F}_\mu = -V_s \vec{\nabla} \bar{\bar{\tau}}_g$	

2.2. SOLID GOVERNING EQUATIONS

In Lagrangian particle tracking, Newton's law of motion is used to describe the motion of individual particles. For a particle i with mass m_i, this reads as:

$$m_i \frac{d\vec{u}_i}{dt} = \sum_j \vec{F}_{ij}^c + \vec{F}_i^{sg} + \vec{F}_i^{grav} \tag{5}$$

Herein, $\vec{F}_{ij}^c$ is the contact force acting on particle i, exerted by particle j or by one of the walls of the domain. $\vec{F}_i^{sg}$ is the total particle-gas interaction force on particle i, i.e. a summation of the drag force, pressure gradient force and viscous force, listed in Table 1. $\vec{F}_i^{grav}$ represents the gravitational force. The contact force between two particles i and j is calculated based on the non-linear Hertz contact model shown in Eq. (6) [49].

$$\vec{F}_{ij}^c = \underbrace{(k_n\vec{\delta}_{n,ij} - \gamma_n\vec{u}_{p,nij})}_{normal\,force\,\vec{F}_n} + \underbrace{(k_t\vec{\delta}_{t,ij} - \gamma_t\vec{u}_{p,tij})}_{tangential\,force\,\vec{F}_t} \tag{6}$$

$$|\vec{F}_t| \leq \mu|\vec{F}_n| \tag{7}$$

The normal contact force, $\vec{F}_n$, and tangential contact force, $\vec{F}_t$, each consist of two terms. The normal contact force comprises of a spring force and a damping force, while the tangential force comprises of a shear and damping force. The tangential contact force is corrected to fulfill the Coulomb criterion depicted in Eq. (7) where μ is the friction factor.

In Eq. (6), k_n and k_t are the normal spring and tangential shear coefficients respectively. $\vec{\delta}_{n,ij}$ is defined as the overlap distance of two particles while $\vec{\delta}_{t,ij}$ corresponds to the tangential displacement between two spherical particles. The tangential displacement is calculated by integrating the relative tangential velocity component of two particles, $\vec{u}_{p,tij}$, at the contact point over time. $\vec{u}_{p,nij}$ is the normal component of the relative velocity between two particles. γ_n and γ_t

are the normal and tangential damping coefficients respectively. k_n, k_t, γ_n and γ_t are calculated from the material properties, according to Eqs. (8) to (13). Herein, Y is the Young modulus, G the shear modulus, ν the Poisson ratio and e the coefficient of restitution.

$$k_n = \frac{4}{3} Y_{eff} \sqrt{R_{eff} \delta_{n,ij}} \; ; \; k_t = 8 G_{eff} \sqrt{R_{eff} \delta_{n,ij}} \tag{8}$$

$$\gamma_n = -2 \sqrt{\frac{5}{6}} \beta \sqrt{S_n m_{eff}} \geq 0 \; ; \gamma_t = -2 \sqrt{\frac{5}{6}} \beta \sqrt{S_t m_{eff}} \geq 0 \tag{9}$$

$$S_n = 2 Y_{eff} \sqrt{R_{eff} \delta_{n,ij}} \; ; S_t = 8 G_{eff} \sqrt{R_{eff} \delta_{n,ij}} \tag{10}$$

$$\beta = \frac{ln(e)}{\sqrt{ln^2(e) + \pi^2}} \tag{11}$$

$$\frac{1}{R_{eff}} = \frac{1}{R_i} + \frac{1}{R_j} \; ; \; \frac{1}{m_{eff}} = \frac{1}{m_i} + \frac{1}{m_j} \; ; \; \frac{1}{Y_{eff}} = \frac{1 - \nu_i^2}{Y_i} + \frac{1 - \nu_j^2}{Y_j} \tag{12}$$

$$\frac{1}{G_{eff}} = \frac{2(2 - \nu_i)(1 + \nu_i)}{Y_i} + \frac{2(2 - \nu_j)(1 + \nu_j)}{Y_j} \tag{13}$$

3. MODEL VALIDATION

3.1. EXPERIMENTAL GSVU SET-UP AND SIMULATION PROCEDURE

The geometry and experimental procedures are described in detail in previous work [39, 50]. Therefore, only a brief description is given here. Figure 1a shows a schematic view of the experimental GSVU geometry. The setup consists of a horizontally placed cylindrical chamber having a height (L_R) of 15 mm and a diameter (D_R) of 80 mm. Eight inclined inlet slots with a width (I_o) of 1 mm are used to feed the process gas. The inclination angle (γ) between the slots and the tangent of the chamber is 10 degrees. Solids are fed via the top plate of the chamber using a dedicated feeding line (not shown on the figure). The design of the GSVU is modular, allowing for easy replacement of the central chamber. Geometric characteristics such as the number, width and inclination of the gas injection slots and the design of the bottom plate can be easily adapted. The simulated geometry, shown in Figure 1b, does not account for the central gas outlet section, equipped with a cyclone, to limit the computational load. Since the influence of the outlet on the bed and gas-phase hydrodynamics inside the chamber is limited, a constant pressure boundary condition of 106 kPa is applied at the outlet. The simulated chamber thus spans a range of radial positions from 15 to 40 mm.

Driven by the gas to solid momentum transfer, the particles inside the central chamber start to rotate. The gas injection velocity is regulated by the size and number of the inlet slots and its volumetric flow rate, while the radial and azimuthal gas injection velocity components are determined by the inclination angle.

The GSVU bottom plate in the experimental setup is made of polycarbonate glass to provide optical access to the particle bed for PIV measurements. Particle azimuthal and radial velocity data near the unit's bottom plate is measured. Other parts of the GSVU are made of steel. In these experiments, aluminum particles with a diameter of 500 micron are loaded in the chamber. As PIV is a non-intrusive, visual technique, only the aluminum particles near the optically accessible bottom wall are observed. More information regarding the PIV setup and its accuracy can be found in previous work [39]. The 2D PIV experimental data, providing both azimuthal and radial particle velocity components, is used for validation of the CFD-DEM model developed in this work.

The experimental GSVU set-up is meshed for use in numerical simulations via the commercial meshing software Pointwise [51]. The mesh consists of 425 920 hexahedral cells, with mesh refining close to the walls and near the inlet slots, as shown in Figure 1c. A mesh independence study is provided in the Supporting Information.

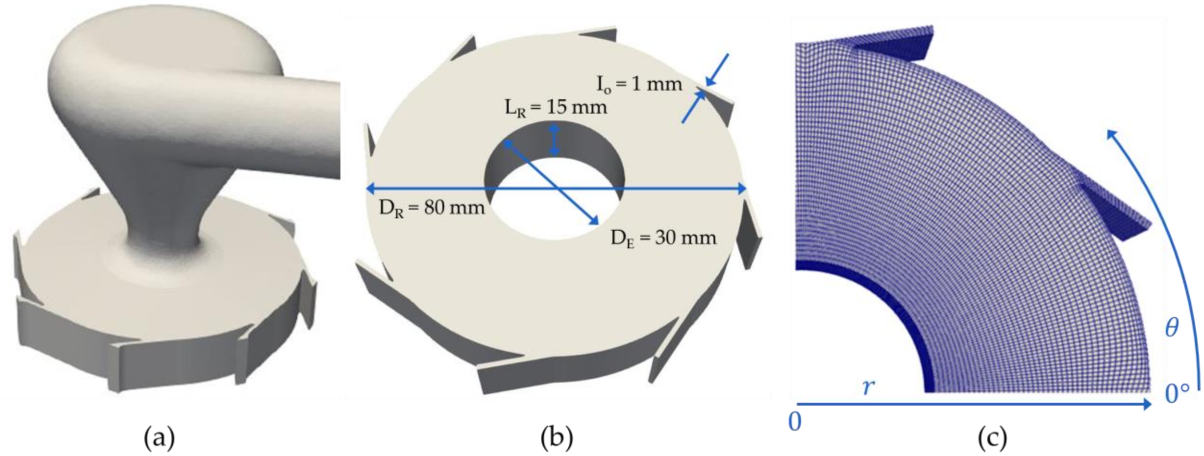

Figure 1: Global view of the GSVU geometry with exhaust section (a), the simulated GSVU geometry (b) and a top view of ¼ of the structured grid with indication of the radial and azimuthal coordinate system (c).

In CFD-DEM, cell sizes often are at least eight times a single particle volume. Accurate modeling of the gas velocity and pressure fields inside the GSVU requires sufficient resolution, resulting in cell volumes ranging from one fourth to four times the particle volume in the considered mesh. Rather than assigning the complete particle volume to the grid cell in which the center of the particle resides, as typically done in CFD-DEM studies, a more sophisticated manner is needed to capture accurate particle volume fraction profiles. In the presented GSVU simulations, each particle is divided in 29 non-overlapping equivolumetric parts. Accounting for the position of the centroids of these parts, the total particle volume is distributed over a number of grid cells.

All relevant geometrical and operating conditions are listed in Table 2. During each CFD timestep, 20 DEM timesteps are performed to accurately resolve the collision behavior between particles. The CFD and DEM timesteps are chosen to have a maximum Courant value of 0.4 while also remaining under 5% of the characteristic collision time for the considered particle type. The pressure implicit split operator (PISO) algorithm is used for pressure-velocity coupling [52]. The simulation proceeds along the following steps. First, the gas velocity field is initialized with a gas-only simulation for a simulated time of 0.01 s. Next, all particles are introduced in the chamber uniformly distributed between a radial position of 30 and 39 mm, with an azimuthal velocity of 5 m/s. After 0.5 seconds of simulated time, a stable bed is obtained and time-averaged data is gathered from 1.5 to 3.0 seconds of simulated time.

Table 2: Overview of geometrical details, operating conditions and numerical settings.

Geometry details	
Diameter	80 mm
Height	15 mm
Number of inlet slots	8
Slot width	1 mm
Inclination angle	10 °
Gas properties	
Composition	air
Temperature	293 K
Outlet pressure	106 kPa
Inlet flow rate	40 Nm^3/h
Density	Ideal gas law
Particle properties	
Material	Aluminum
Density	2700 kg/m^3
Diameter	500 µm
Solids loading	10.7 g
Number of particles	60 513
Temperature	293 K
Collision model	Hertzian
Young modulus	5 MPa
Poisson ratio	0.45
Particle-particle restitution coefficient	0.97
Particle-wall restitution coefficient	0.2-0.6
Particle-particle friction coefficient	1.0
Particle-wall friction coefficient	0.6
Solution settings	
CFD timestep	$8 \cdot 10^{-7}$ s
DEM timestep	$4 \cdot 10^{-8}$ s
Spatial discretization	Second-order
Temporal discretization	Euler (first order)

3.2. Validation Study

The model described above can only be used for reactor design after a thorough validation study. The results of such a study focusing on the determination of minimum fluidization velocities in the gravitational field is provided in the Supporting Information. In this section, a second validation study performed within the GSVU geometry is presented. Herein, experimental and simulated local particle velocity fields near the transparent bottom plate are compared. This section focuses on the direct comparison between experimental and simulation results. The solid and gas phase hydrodynamics are discussed next.

Except for the density and diameter, the intrinsic material properties of the particles are not known. Consequently, the particle-wall and inter-particle friction factors and restitution coefficients have unidentified values. However, these parameters partly determine the particle-wall and inter-particle collision characteristics. Therefore, these parameter values are tuned to increase the model performance in the GSVU. In a first set of CFD-DEM simulations, the friction factors are varied based on reported literature values [53]. It was concluded that a friction factor of 1.0 for inter-particle interactions and a friction factor of 0.6 for particle-side wall and particle-bottom plate interactions give rise to the best results. In a next step, the particle-particle restitution coefficient is set at 0.97. This value is based on preliminary CFD-DEM simulations to predict accurate bed expansion in the GSVU. The particle-side wall and particle-bottom plate restitution coefficients are varied between a value of 0.2 and 0.6, with steps of 0.1. This range is supported by restitution coefficients proposed by Blawucki et al. [54] and Constantinides et al. [55] for aluminum alloys. The choice to opt for a lower value of the particle-wall restitution coefficient compared to the inter-particle restitution coefficient stems from the difference in relative impact velocity. At higher impact velocities, the restitution coefficient typically has a lower value, as shown by Seifried et al [56]. In what follows, simulation results will be referred to by using the applied value for the particle-wall restitution coefficient e. The presented results are limited to the simulations with values for e of 0.2, 0.3 and 0.4. When the restitution coefficient further increases to 0.6, the same trends hold as when the particle-wall restitution coefficient increases from 0.2 to 0.4. As the difference between simulation results and experimental data further increases, these results are not presented.

Figure 2 shows 2D plots of the time-averaged azimuthal particle velocity for restitution coefficient values of 0.2, 0.3 and 0.4 alongside the experimental data. Reported CFD-DEM particle velocity data is gathered by averaging the time-averaged particle velocity between a reactor height of 0 and 1 mm, similarly to the penetration range of PIV measurements. Radial positions are limited between a value of 35 and 40 mm since this is the region in which the particle bed is located. In all 2D plots presented in this work, gas inlet slots are located at azimuthal coordinates of 0, 45 and 90 degrees, as previously shown in Figure 1b. The overall conclusion for Figure 2 is that the CFD-DEM calculated velocity fields capture the regions of high and low azimuthal velocity accurately and that the simulation results describe the experimental data better when the particle-wall restitution coefficient lowers. The latter is supported by the value of the minimum and maximum azimuthal particle velocity, also presented in Figure 2. The regions of high azimuthal velocity are located in zones of intense momentum transfer between gas and particles, i.e. after passing an inlet slot.

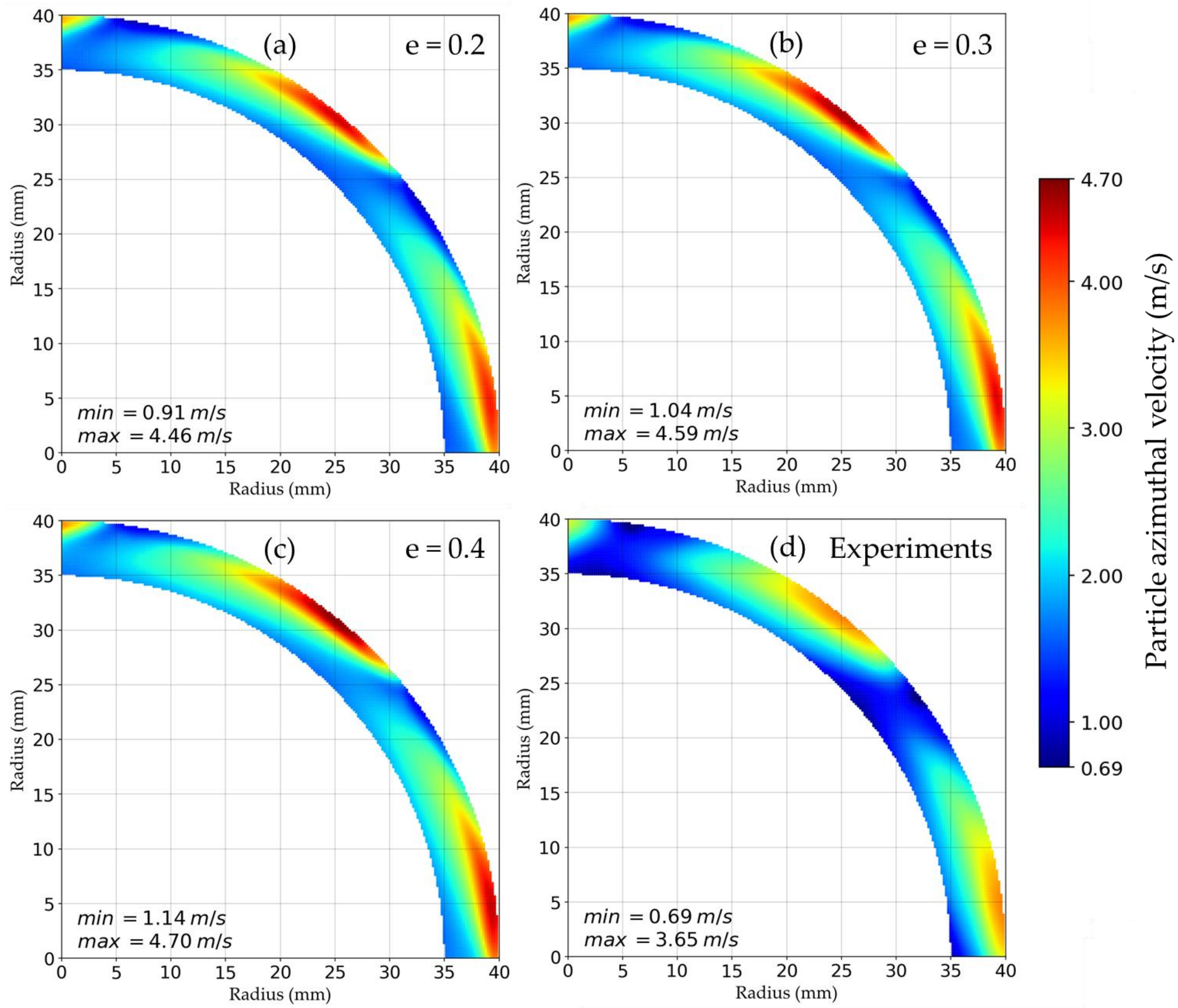

Figure 2: Time-averaged 2D azimuthal particle velocity fields at the bottom of the chamber, obtained via CFD-DEM simulations (a-c) and experimentally captured via PIV (d).

A 2D plot of the calculated time-averaged radial particle velocity component for all three restitution coefficient values of 0.2, 0.3 and 0.4 alongside the experimental data is shown in Figure 3. Again, the zones with high and low radial velocity components are described well in a qualitative manner. Particles move radially inwards after passing an inlet slot due to the radial component of the gas inlet velocity of which the magnitude is determined by the inclination angle of the slots. Contrary to the results for azimuthal particle velocity presented in Figure 2, Figure 3 shows that the CFD-DEM calculated fields for the radial velocity components describe the experimental data better when the particle-wall restitution coefficient increases.

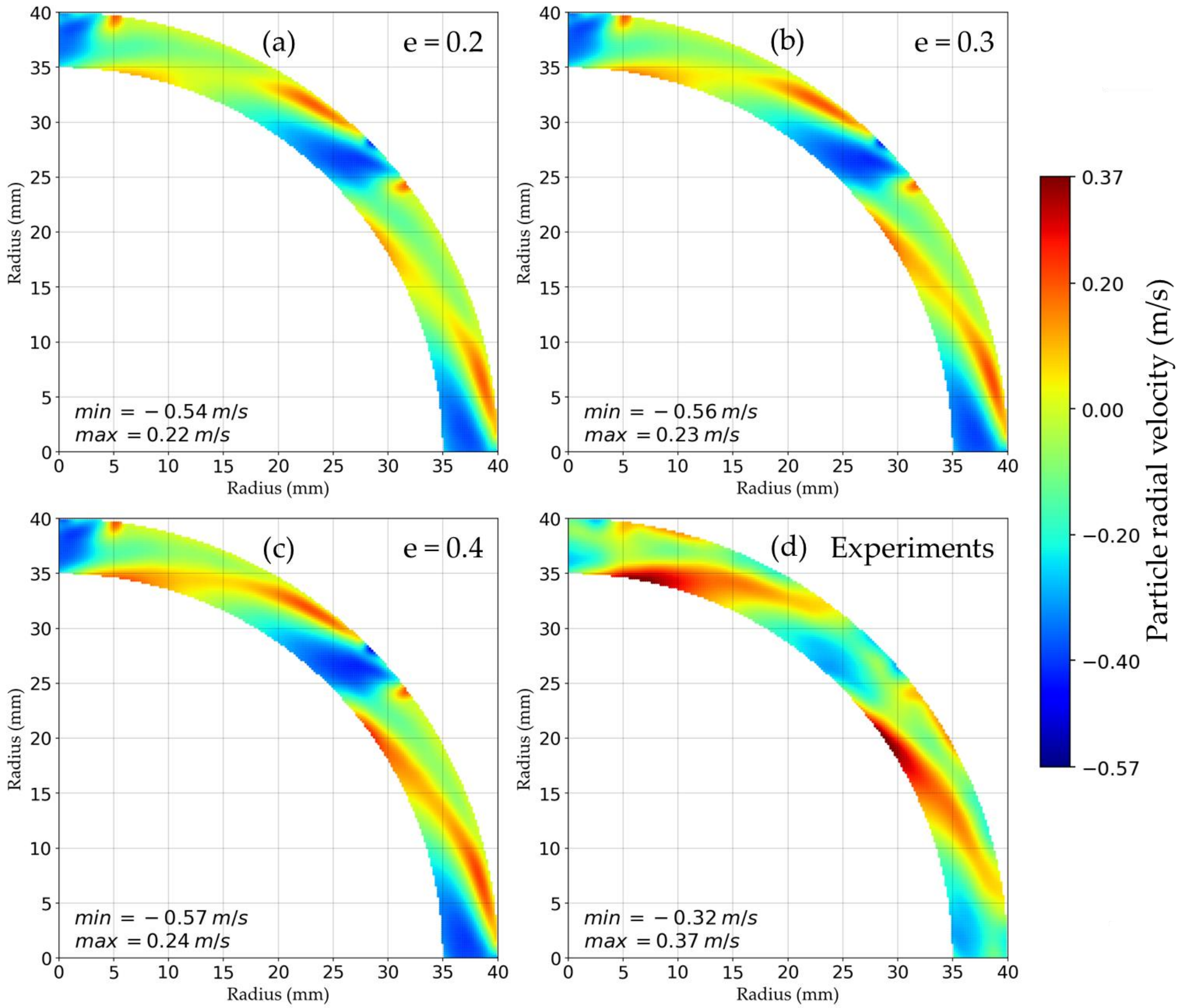

Figure 3: Time-averaged 2D radial particle velocity fields at the bottom of the chamber, obtained via CFD-DEM simulations (a-c) and experimentally captured via PIV (d).

The presented 2D plots provide qualitative information on global trends. A more quantitative analysis is made with the use of parity diagrams. Figure 4 shows parity diagrams for both the azimuthal and radial particle velocity components based on the data presented in Figure 2 and Figure 3. In the parity diagrams for azimuthal velocity components (Figure 4 a-c), the top and bottom red lines indicate where the simulated and experimentally measured azimuthal particle velocity components differ by 0.5 m/s. The top and bottom red lines in the parity diagrams for the radial particle velocity (Figure 4 d-f) indicate a difference of 0.1 m/s. The performance of the CFD-DEM simulations performed with varying restitution coefficients is compared based on different metrics. The mean absolute error (MAE) and root mean square error (RMSE) are added in the parity diagrams in the top left corner. As already mentioned when discussing Figure 2, the descriptive performance for the azimuthal particle velocity components improves upon lowering the value of the particle-wall restitution coefficient. The inverse observation is made for the radial velocity components, as already mentioned when discussing Figure 3. This conclusion is also supported by the MAE and RMSE values. However, for all values of the particle-wall restitution coefficient the lowest and highest azimuthal particle velocity components are overestimated by the model. An overprediction of the lowest azimuthal velocities was already reported by Vandewalle et al. [18] making use of an Eulerian-Eulerian model. In Figure 4a-c, it is observed that a decrease of the restitution coefficient brings the calculated azimuthal particle velocity component closer to the experimental values in the region of 1.5 m/s to 3.0 m/s. The value of the restitution coefficient mainly influences the positive values of the radial particle velocity component. Simulated radial particle velocity components above 0.1 m/s come closer to the experimentally determined values for an increase in particle-wall restitution coefficient.

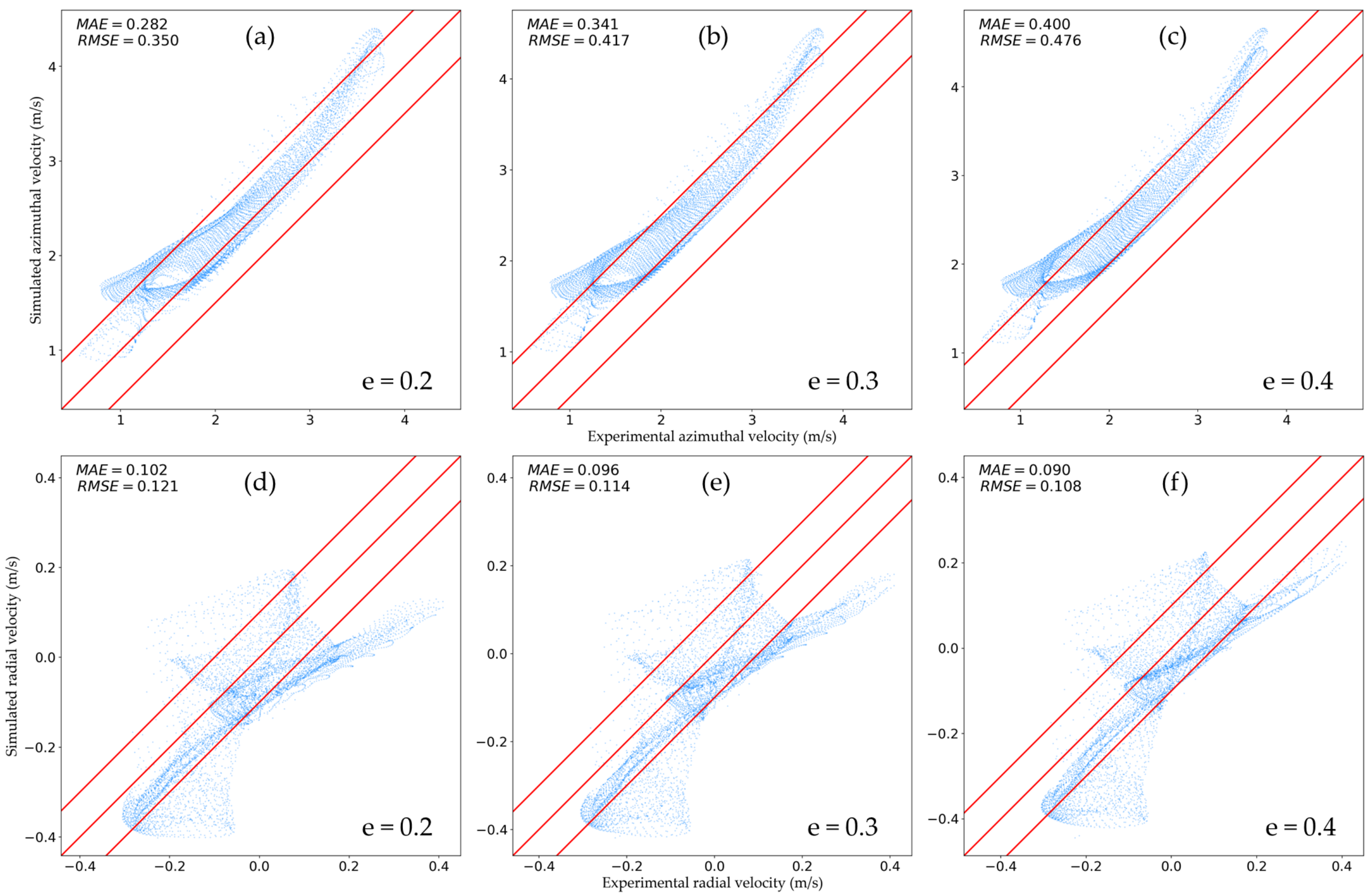

Figure 4: Parity diagrams for time-averaged azimuthal particle velocity (a-c) and radial particle velocity (d-f) components for a particle-wall restitution coefficient of 0.2 (a, d), 0.3 (b, e) and 0.4 (c, f).

In Figure 5, the time-averaged simulated particle velocity components in between two consecutive inlet slots are sampled as a function of the relative azimuthal coordinate between two inlet slots at two radial positions. The azimuthal and radial particle velocity components at radial positions of 37 and 39 mm are shown along with the experimental data, including experimental error bars. These radial positions are selected because they are located in two distinctly different regions. At a radial position of 37 mm bulk bed behavior is observed. At 39 mm, the influence of the side wall and gas inlet slot on the velocity values can be analyzed. From Figure 5, it can be concluded that, considering the experimental uncertainty on the PIV measurements, the CFD-DEM model performs well quantitatively. An overprediction of the azimuthal particle velocity component for all values of the particle-wall restitution coefficients is observed when approaching an inlet slot, i.e. at a relative azimuthal coordinate of 0.9 and 0.8 at a radial position of 37 and 39 mm respectively, as shown on Figure 5a and b. However, the location of the maximum azimuthal particle velocity component is very well-predicted. The location shifts from a relative azimuthal coordinate of 0.2, i.e. near an inlet slot, for a radial position of 39 mm to a central position of 0.4 for a radial position of 37 mm.

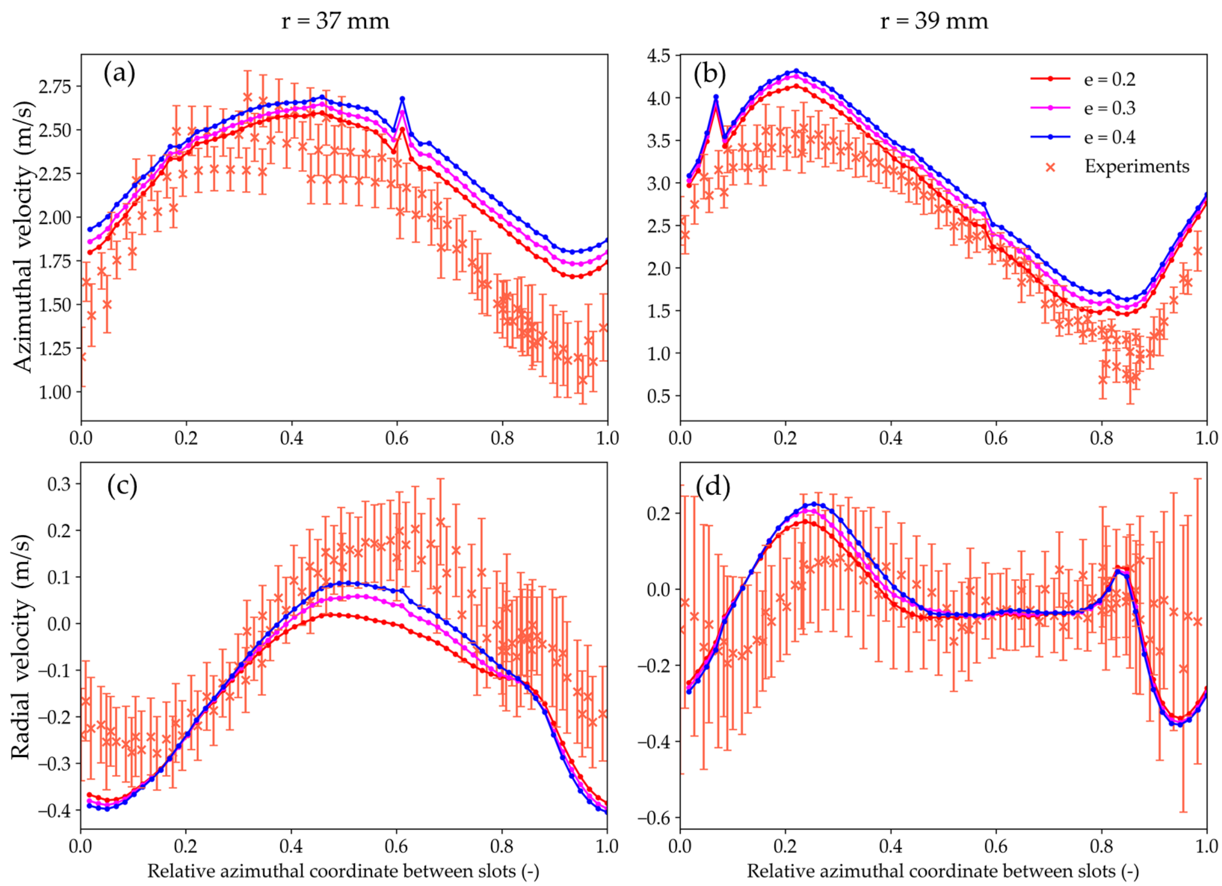

Figure 5: Time-averaged azimuthal (a-b) and radial (c-d) particle velocity component profiles at radial positions r = 37 mm (a, c) and r = 39 mm (b, d) for different particle-wall restitution coefficients.

From Figure 5c and d, it is concluded that in the middle of two inlet slots, at a radial position of 37 mm, the CFD-DEM model slightly underpredicts the radial particle velocity component for all particle-wall restitution coefficient values used. However, this underestimation is minimal. Moreover, the change in radial velocity when approaching an inlet slot is accurately captured. Both the central flattening and the sudden drop in radial particle velocity at a relative azimuthal coordinate of 0.8 are correctly described. At a radial position of 39 mm, the spike and sudden decrease in radial particle velocity component at relative azimuthal coordinates between 0.8 and 0.95 are captured by the CFD-DEM model.

From Figures 2 to 5, it can be concluded that adequate quantitative predictions of both azimuthal and radial particle velocity components are obtained for a particle-wall restitution coefficient of 0.3. In the remaining part of this work, results obtained using this value are presented.

4. RESULTS AND DISCUSSION

4.1. SOLID PHASE HYDRODYNAMICS

Now that the model is validated, it can be used to evaluate some hydrodynamic features that cannot easily be measured experimentally. This includes a more elaborate analysis of the particle packing in the bed, which is closely related the particle velocity fields mentioned in the validation study above.

In Figure 2, it was shown that the highest azimuthal particle velocity components are observed downstream of an inlet slot due to intense momentum transfer from gas to particles. The particle azimuthal velocity decreases when particles approach an inlet slot. The latter is accompanied by particle build-up as will be discussed later in this section. It was shown in Figure 5a and b that the position of maximal particle azimuthal velocity shifts towards a position further downstream of the inlet slot when the radial position lowers. The magnitude of this shift is related to the inclination angle of the gas inlet slots. With an increase in inclination angle, the shift becomes less pronounced and simultaneously, the azimuthal momentum transfer from gas to particles decreases.

As observed in Figure 3, downstream of an inlet slot, the particles move radially inwards due to the momentum transfer from the gas phase injected in the chamber with an inclination angle of 10°. Due to the relatively high radial component of the gas injection velocity, the radially oriented drag force dominates the centrifugal force at an inlet slot. For azimuthal positions between two consecutive inlet slots, the centrifugal force dominates the drag force and particles move radially outward. When approaching the next inlet slot, particles build up and are forced radially inward.

Although the centrifugal forces largely outweigh the gravitational force on individual particles, the effect of gravity on bed thickness cannot be neglected, as observed in Figure 6. Bed thickness increases when closing in to the bottom plate. Along the azimuthal coordinate, high variations in bed thickness and particle volume fractions are observed as well. These phenomena are discussed in this section.

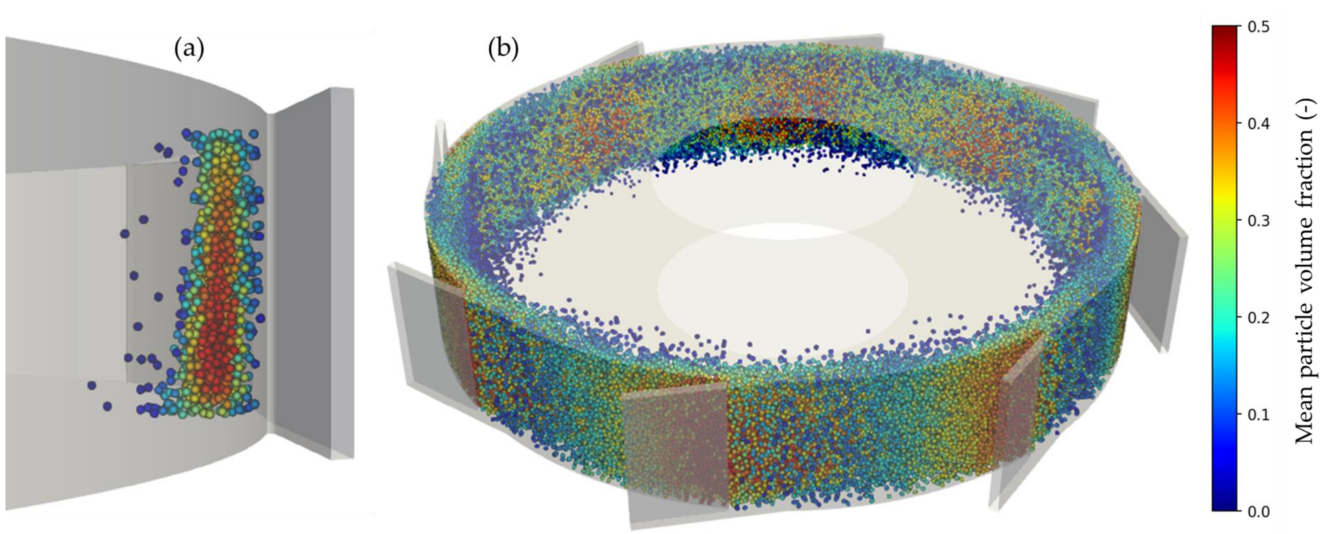

Figure 6: Snapshot of a slice (a) and global overview (b) of the particle bed. Particles are colored based on mean particle volume fraction in the grid cell.

Figure 7a-c displays 2D plots of the time-averaged particle volume fraction at three different reactor heights: at the bottom and top plate and at mid-height of the chamber. The axial profiles of particle volume fraction at radial positions of 37 and 39 mm at three different relative azimuthal coordinates are shown in Figure 7d. From the 2D plots in Figure 7, it is concluded that the particle bed is less dense near the top (14 mm) and bottom (1 mm) plate compared to what is observed at mid-height (7.5 mm). However, the total bed thickness, i.e. how far the particle bed reaches radially inwards, is largest near the bottom plate and decreases along the chamber height. The lower particle volume fraction at the bottom plate stems from non-ideal particle packing close to a flat plate. On average, more gas-phase momentum is thus transferred to a single particle, diluting the bed close to the bottom plate.

The latter is confirmed by the axial profiles of the particle volume fraction shown in Figure 7d. Near the wall, the bed is more uniform along the chamber height due to the considerably more intense momentum transfer from gas to particles. When approaching an inlet slot, build-up of particles near the wall is clearly observed by the profiles for increasing relative azimuthal coordinate. There are considerable particle volume fraction gradients near the bottom and top plate due to gas by-pass and bed dilution. The highest particle volume fractions are found at a height of approximately 3 mm. Next, the particle volume fraction decreases monotonously with increasing height for all three relative azimuthal coordinates. At a radial position of 37 mm, the overall maximum in particle volume fraction is calculated at an inlet slot, i.e. at a relative azimuthal coordinate of 0.

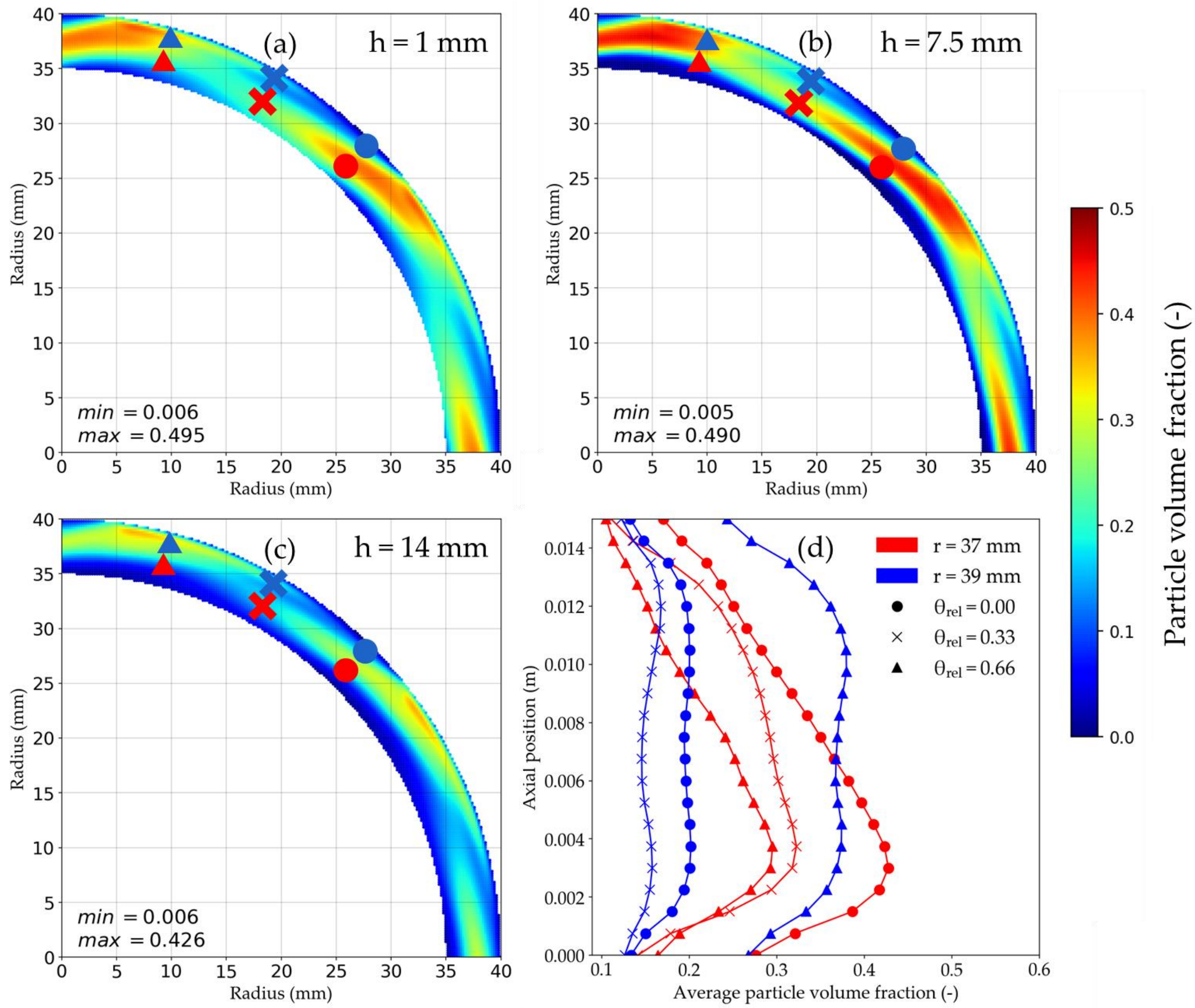

Figure 7: Time-averaged particle volume fraction at axial reactor heights of 1 (a), 7.5 (b) and 14 (c) mm. The axial particle volume fraction profile is shown at radial positions of 37 and 39 mm at 3 different relative azimuthal coordinates (d). Sampling locations of the three azimuthal coordinates are indicated at each axial height.

The maximum particle volume fraction in the bulk of the bed (i.e. at 37 mm) is located around 3 mm above the bottom plate. Therefore, in Figure 8, profiles of the particle volume fraction, at radial positions of 37 and 39 mm, are shown at reactor heights of 3, 7.5 and 12 mm as a function of the relative azimuthal coordinate. Similar profiles are obtained at the different reactor heights. The minima and maxima in particle volume fraction are located at almost the same relative azimuthal coordinate for each reactor height. Only the minimum value at a radial position of 37 mm shifts to higher relative azimuthal coordinates for an increase in chamber height. It is clear that the variation in particle volume fraction between different chamber heights closer to the wall is found to be smaller as compared to the bulk of the bed.

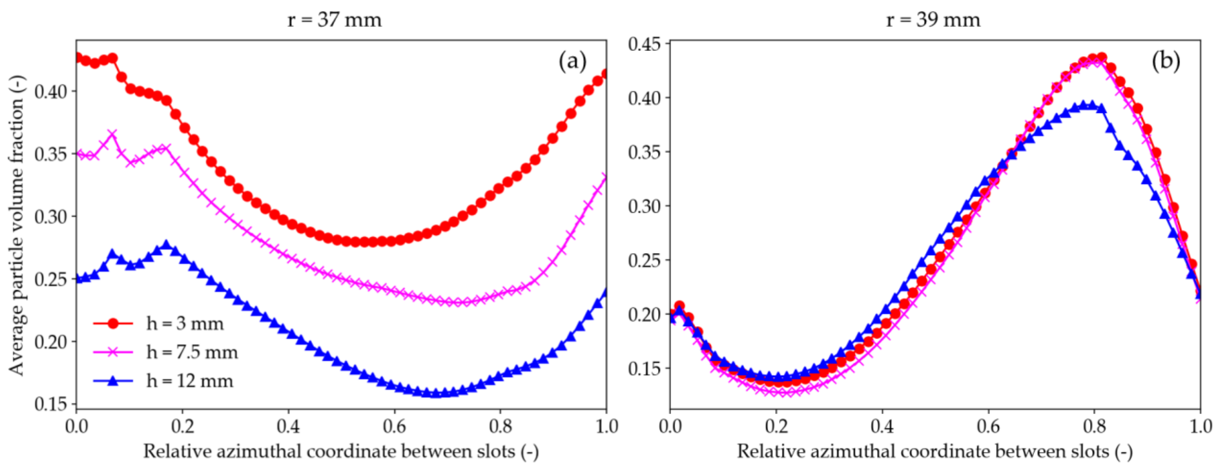

Figure 8: Particle volume fractions at three different axial positions (3, 7.5 and 12 mm reactor height) at both a radial position of 37 mm (a) and 39 mm (b)

One of the strong suits of CFD-DEM is its ability to track individual particle positions. Figure 9 shows the position of a single particle over the considered simulated time. Clearly, particle movement in the bed is turbulent, highlighted via the large oscillations in both the axial and radial position. Individual particles move from the outer edge of the bed to the inner edge of the bed around twice per second at these conditions, accompanied by micro-mixing in between these macro movements. Particle movement along the axial height of the unit is, due to the absence of an axial component in the gas inlet flow, less turbulent. However, individual particles are still found to move from the bottom to the top of the unit and vice versa, albeit at a lower frequency. In view of the highly exothermal OCM process, this intense intra-bed particle mixing is highly beneficial for operation in the GSVU. Hot catalyst particles can be transported from one edge of the bed to the other, creating a pseudo-isothermal fluidized bed due to thermal back-mixing. When process gas is injected at a sufficiently low temperature, autothermal OCM operation of the GSVU becomes possible. Herein, heat generated due to the OCM process is used to heat the process gas. However, the possibility for autothermal operation strongly depends on the operation conditions and the associated bifurcation curves showing zones of extinction and ignition of the particle bed. Under optimal operating conditions, no external heating or cooling would be necessary for OCM in the GSVU.

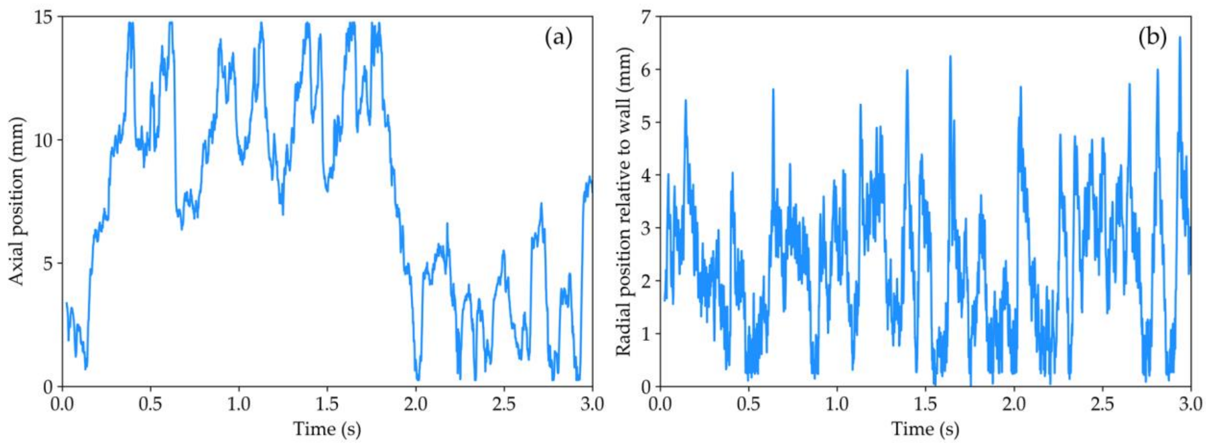

Figure 9: Single particle position over the considered simulated time: (a) axial position and (b) radial position relative to the side wall of the GSVU.

Several measures can be taken to reduce the effect of gravity on bed thickness or to realize a more uniform particle volume fraction along the azimuthal coordinate. For example, a chamber with a higher number of inlet slots while maintaining the same gas superficial inlet velocity could be used. This increases the gas volumetric flow rate. If the gas volumetric flow rate must not be increased, the number of inlet slots can be increased while reducing the slot width to maintain a similar gas superficial inlet velocity. A third option is decreasing the slot width for a given number of inlet slots and gas volumetric flow rate, increasing the gas superficial inlet velocity. Intelligent design of the shape of the inlet slot could also improve bed uniformity, a measure of which the impact will be noticeable on individual particles near the inlet slots, for which detailed CFD-DEM are deemed necessary. Assessing the impact of several measures will be part of future work.

4.2. Gas-phase hydrodynamics

The above discussion handles the flow characteristics of the particle bed since the particle velocity fields are essential for the validation of the CFD-DEM model used in this work. However, high heat and mass transfer rates in the GSVU are primarily related to high gas-solid slip velocities. Figure 10 shows two different sets of time-averaged gas velocity streamlines inside the GSVU. In Figure 10a, the blue and red streamlines correspond to gas flowing in the bottom and top half of the GSVU respectively showing that axial mixing in the gas-phase is very low. Vortex generation is suppressed due to momentum transfer from gas to particles. As streamlines extend from inflow to outflow, the rotation of gas in the lower part of the chamber is lowest. This confirms that total momentum transfer from gas to particles decreases with chamber height, as discussed above. In the second set, the streamlines are colored based on the time-averaged gas velocity magnitude. Figure 10b shows that, upon entering the chamber, the gas velocity is reduced by over 90% due to momentum transfer to the particles.

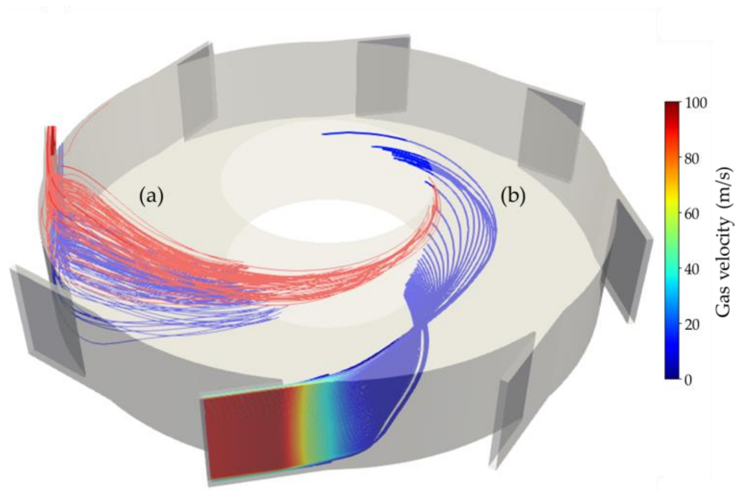

Figure 10: Streamlines of time-averaged gas velocity (a) colored by reactor height where blue and red represent the bottom and top half of the reactor unit respectively and (b) colored by mean gas velocity magnitude.

Most of the gas has left the chamber before reaching the azimuthal position of the next inlet slot. The limited gas rotation in the chamber results in a small average residence time and a narrow residence time distribution. Figure 11 displays the residence time distribution at two radial positions in non-dimensional time. A scalar transport equation is solved on the frozen time-averaged gas velocity field while monitoring the average tracer concentration at two different cylindrical surfaces over time. The cylindrical surface at a radial position of 32.5 mm corresponds to a position downstream of the particle bed. A residence time distribution corresponding to a Péclet number of 10 and 47 is obtained downstream of the bed and at the outlet of the chamber respectively, highlighting that the distribution is indeed narrow. The narrow low-mean residence time distribution makes the GSVU an ideal reactor technology for processes in which secondary reactions are undesired, e.g. biomass pyrolysis [20, 50] and OCM [18]. More information regarding the determination of this residence time distribution is provided in the Supporting Information.

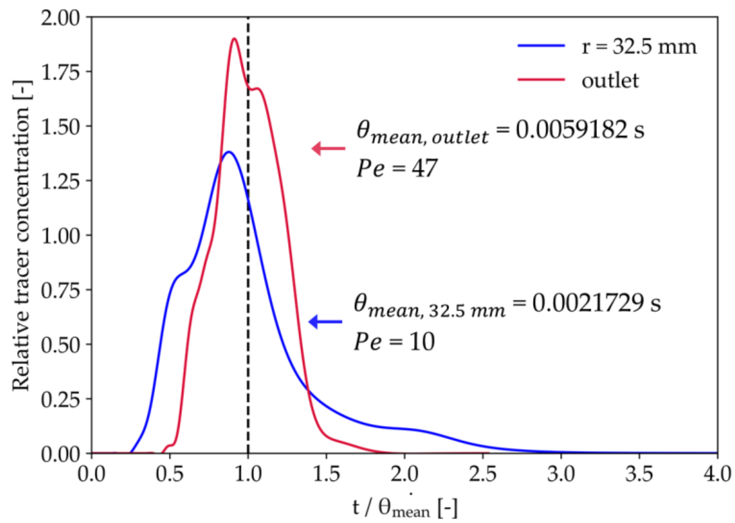

Figure 11: Gas-phase residence time distribution of a tracer at two radial positions (r = 32.5 mm and at the outlet, i.e. r = 15 mm). Mean residence times as well as Péclet numbers determined based on the non-dimensional residence time distribution are indicated.

Figure 12 displays the simulated gas-solid slip velocities in both the azimuthal and radial directions obtained at mid-height of the chamber for three different radial positions. The azimuthal slip velocity is highest close to the circumferential wall and lowers with a decrease in radial position. This decrease in gas-solid slip velocity is induced by the gas transferring almost all of its azimuthal momentum to the particles. The inverse holds for the radial gas-solid slip velocity, although the variation between different radial positions is lower. This behavior can be explained using Figure 10. Upon further penetrating the bed, the radial gas velocity component becomes more dominant. Maximal slip velocities are obtained downstream of an inlet slot, quickly lowering due to the gas-particle contact and associated momentum transfer. Due to particle slowdown and the jet-like inlet slots, high slip velocities are realized as well when approaching an inlet slot.

In gravitational fluidized beds, the maximum obtainable gas-solid slip velocity, i.e., before entrainment occurs, is equal to the terminal free falling velocity of the particle. The aluminum particles considered here have a theoretical free falling velocity of 3.4 m/s [39]. Clearly, this value is largely exceeded at several positions in the GSVU bed. In the high slip velocity regions, over 7 times the maximum gravitational slip velocity is realized. Heat and mass transfer rates will thus largely exceed those obtainable in a gravitational fluidized bed at several positions in the GSVU.

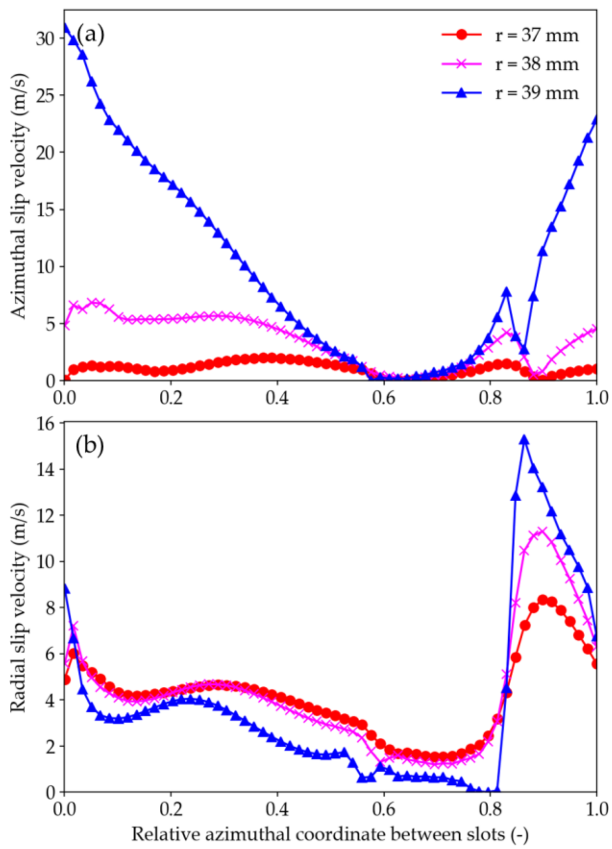

Figure 12: Gas-solid azimuthal (a) and radial (b) gas-solid slip velocities at a chamber height of 7.5 mm.

5. Conclusions

An in-house developed CFD-DEM model is validated in a rotating fluidized bed in a static geometry, i.e. a so-called gas-solid vortex unit, designed in view of intensifying heterogeneously catalyzed gas-solid processes. 2D particle image velocimetry data on local radial particle and azimuthal velocity are used for model validation inside the GSVU geometry. This data is obtained via optical access through the unit's bottom plate. Thorough validation is performed over the complete 2D bottom plane of the particle bed, showing good qualitative and quantitative performance of the CFD-DEM model. Distinct zones of high and low azimuthal and radial particle velocities are captured accurately. Only a small overprediction on the azimuthal velocity and a minor underprediction of the radial particle velocity in the bulk of the bed is observed. Furthermore, the flow characteristics of the gas and solid phase are discussed in regions inaccessible to non-intrusive measurement techniques. This includes the particle volume fraction profiles at different zones of the reactor as well as gas velocities. It is shown that a narrow low-averaged gas-phase residence time distribution is obtained in the GSVU. For process intensification purposes, the azimuthal and radial gas-solid slip velocities are determined at mid-height of the reactor chamber. These gas-solid slip velocities greatly exceed the maximum slip velocity of the aluminum particles achievable in the gravitational field in different zones, up to over a factor 7. A challenge that remains is minimizing the effect of gravity on the bed thickness, but our simulations help to come up with a series of solutions to resolve this. This makes the GSVU a perfect candidate for the intensification of numerous processes. The CFD-DEM model validated in this work can provide a powerful tool to further design the GSVU and enhance its process intensifying potential.

Nomenclature

Roman

d	Diameter	m
e	Restitution coefficient	$-$
F	Force	N
g	Gravitational constant	$m\ s^{-2}$
G	Shear modulus	Pa
I	Unit tensor	$-$
k	Spring constant	$N\ m^{-1}$
K	Momentum exchange coefficient	$kg\ m^{-3}\ s^{-1}$
m	Mass	kg
p	Pressure	Pa
R	Radius	m
Re	Reynolds number	$-$
t	Time	s
u	Velocity	$m\ s^{-1}$
V	Volume	m^3
Y	Young modulus	Pa

Greek

γ	Inclination	$^\circ$
γ	Damping factor	$-$
δ	Overlap	m
ε	Volume fraction	$-$
θ	Azimuthal angle	rad
θ	Residence time	s
μ	Dynamic viscosity	$Pa\ s$
μ	Friction factor	$-$
ρ	Density	$kg\ m^{-3}$
τ	Stress	Pa

Sub/superscripts

c	Contact
cell	CFD cell
d	Drag
eff	Effective

g	Gas phase
grav	Gravitational
gs	Gas-solid
i	Index
j	Index
mean	Averaged
n	Normal
o	Slot opening
p	Pressure
R	Reactor
s	Solid
t	Tangential
t	Turbulent
w	Wall
μ	Viscous

ACRONYMS

CFD	Computational Fluid Dynamics
DEM	Discrete Element Method
FBR	Fluidized bed reactor
GSVU	Gas-solid vortex unit
OCM	Oxidative Coupling of Methane
PI	Process Intensification
PIV	Particle Image Velocimetry
RFB	Rotating Fluidized Bed
RFB-SG	Rotating Fluidized Bed in a Static Geometry

ACKNOWLEDGMENTS

Florian Wéry acknowledges financial support from a doctoral fellowship from the Fund for Scientific Research Flanders (FWO) under application number 1S97521N and 1248922N. The computational resources (Stevin Supercomputer Infrastructure) and services used in this work were provided by the VSC (Flemish Supercomputer Center), funded by Ghent University, FWO and the Flemish Government – department EWI. The research leading to these results has also received funding from the European Research Council (ERC) under the European Union's Seventh Framework Programme (FP7/2007-2013)/ERC grant agreement no. 818607 (OPTIMA).

REFERENCES

[1] E.T.C. Vogt, B.M. Weckhuysen, Fluid catalytic cracking: recent developments on the grand old lady of zeolite catalysis, Chem. Soc. Rev. 44 (2015) 7342-7370. doi.org/10.1039/C5CS00376H.

[2] J. Kopyscinski, T.J. Schildhauer, S.M.A. Biollaz, Fluidized-Bed Methanation: Interaction between Kinetics and Mass Transfer, Ind. Eng. Chem. Res. 50 (2011) 2781-2790. doi.org/10.1021/ie100629k.

[3] M. Martinelli, M.K. Gnanamani, S. LeViness, G. Jacobs, W.D. Shafer, An overview of Fischer-Tropsch Synthesis: XtL processes, catalysts and reactors, Appl. Catal., A 608 (2020) 117740. doi.org/10.1016/j.apcata.2020.117740.

[4] P. Cai, L. Chen, J. van Egmond, M. Tilston, Some recent advances in fluidized-bed polymerization technology, Particuology 8 (2010) 578-581. doi.org/10.1016/j.partic.2010.09.006.

[5] M. Menéndez, J. Herguido, A. Bérard, G.S. Patience, Experimental methods in chemical engineering: Reactors—fluidized beds, Can. J. Chem. Eng. 97 (2019) 2383-2394. doi.org/10.1002/cjce.23517.

[6] X.-Z. Chen, D.-P. Shi, X. Gao, Z.-H. Luo, A fundamental CFD study of the gas–solid flow field in fluidized bed polymerization reactors, Powder Technol. 205 (2011) 276-288. doi.org/10.1016/j.powtec.2010.09.039.

[7] R. Sivakumar, R. Saravanan, A. Elaya Perumal, S. Iniyan, Fluidized bed drying of some agro products – A review, Renewable Sustainable Energy Rev. 61 (2016) 280-301. doi.org/10.1016/j.rser.2016.04.014.

[8] N. Fernando, M. Narayana, W.A.M.K.P. Wickramaarachchi, The effects of air velocity, temperature and particle size on low-temperature bed drying of wood chips, Biomass Convers. Biorefin. 8 (2018) 211-223. doi.org/10.1007/s13399-017-0257-7.

[9] H. Chen, X. Liu, C. Bishop, B.J. Glasser, Fluidized bed drying of a pharmaceutical powder: A parametric investigation of drying of dibasic calcium phosphate, Drying Technol. 35 (2017) 1602-1618. doi.org/10.1080/07373937.2016.1265552.

[10] C.A.M. da Silva, O.P. Taranto, Real-Time Monitoring of Gas–Solid Fluidized-Bed Granulation and Coating Process: Evolution of Particle Size, Fluidization Regime Transitions, and Psychometric Parameters, Drying Technol. 33 (2015) 1929-1948. doi.org/10.1080/07373937.2015.1076000.

[11] Z. Li, J. Li, X. Liu, R. Chen, Progress in enhanced fluidization process for particle coating via atomic layer deposition, Chem. Eng. Process. 159 (2021) 108234. doi.org/10.1016/j.cep.2020.108234.

[12] Y.T. Makkawi, P.C. Wright, Fluidization regimes in a conventional fluidized bed characterized by means of electrical capacitance tomography, Chem. Eng. Sci. 57 (2002) 2411-2437. doi.org/10.1016/S0009-2509(02)00138-0.

[13] G.-H. Qian, I. Bágyi, I.W. Burdick, R. Pfeffer, H. Shaw, J.G. Stevens, Gas–solid fluidization in a centrifugal field, AIChE J. 47 (2001) 1022-1034. doi.org/10.1002/aic.690470509.

[14] M.H. Shi, H. Wang, Y.L. Hao, Experimental investigation of the heat and mass transfer in a centrifugal fluidized bed dryer, Chem. Eng. J. 78 (2000) 107-113. doi.org/10.1016/S1385-8947(00)00148-0.

[15] A. Dutta, R.P. Ekatpure, G.J. Heynderickx, A. de Broqueville, G.B. Marin, Rotating fluidized bed with a static geometry: Guidelines for design and operating conditions, Chem. Eng. Sci. 65 (2010) 1678-1693. doi.org/10.1016/j.ces.2009.11.013.

[16] J. De Wilde, Gas–solid fluidized beds in vortex chambers, Chem. Eng. Process. 85 (2014) 256-290. doi.org/10.1016/j.cep.2014.08.013.

[17] W. Rosales Trujillo, J. De Wilde, Fluid catalytic cracking in a rotating fluidized bed in a static geometry: a CFD analysis accounting for the distribution of the catalyst coke content, Powder Technol. 221 (2012) 36-46. doi.org/10.1016/j.powtec.2011.12.015.

[18] L.A. Vandewalle, A. Gonzalez-Quiroga, P. Perreault, K.M. Van Geem, G.B. Marin, Process Intensification in a Gas–Solid Vortex Unit: Computational Fluid Dynamics Model Based Analysis and Design, Ind. Eng. Chem. Res. 58 (2019) 12751-12765. doi.org/10.1021/acs.iecr.9b01566.

[19] R.W. Ashcraft, J. Kovacevic, G.J. Heynderickx, G.B. Marin, Assessment of a Gas–Solid Vortex Reactor for SO2/NOx Adsorption from Flue Gas, Ind. Eng. Chem. Res. 52 (2013) 861-875. doi.org/10.1021/ie300399w.

[20] R.W. Ashcraft, G.J. Heynderickx, G.B. Marin, Modeling fast biomass pyrolysis in a gas–solid vortex reactor, Chem. Eng. J. 207-208 (2012) 195-208. doi.org/10.1016/j.cej.2012.06.048.

[21] W. Zhang, A Review of Techniques for the Process Intensification of Fluidized Bed Reactors, Chin. J. Chem. Eng. 17 (2009) 688-702. doi.org/10.1016/S1004-9541(08)60264-5.

[22] V. Francia, K. Wu, M.-O. Coppens, Dynamically structured fluidization: Oscillating the gas flow and other opportunities to intensify gas-solid fluidized bed operation, Chem. Eng. Process. 159 (2021) 108143. doi.org/10.1016/j.cep.2020.108143.

[23] J. Kim, G.Y. Han, Effect of agitation on fluidization characteristics of fine particles in a fluidized bed, Powder Technol. 166 (2006) 113-122. doi.org/10.1016/j.powtec.2006.06.001.

[24] R. Samson, C.E. Brakel, A.M. Scott, K. Chandrasekharan, P. Veenstra, A bubble model describing the influence of internals on gas fluidization, Chem. Eng. Sci. 43 (1988) 2215-2220. doi.org/10.1016/0009-2509(88)87106-9.

[25] H. Goyal, T.-Y. Chen, W. Chen, D.G. Vlachos, A review of microwave-assisted process intensified multiphase reactors, Chem. Eng. J. 430 (2022) 133183. doi.org/10.1016/j.cej.2021.133183.

[26] V.V. Idakiev, S. Marx, A. Roßau, A. Bück, E. Tsotsas, L. Mörl, Inductive heating of fluidized beds: Influence on fluidization behavior, Powder Technol. 286 (2015) 90-97. doi.org/10.1016/j.powtec.2015.08.003.

[27] M.J. Espin, M.A.S. Quintanilla, J.M. Valverde, Magnetic stabilization of fluidized beds: Effect of magnetic field orientation, Chem. Eng. J. 313 (2017) 1335-1345. doi.org/10.1016/j.cej.2016.11.023.

[28] Y. Mawatari, T. Koide, Y. Tatemoto, T. Takeshita, K. Noda, Comparison of three vibrational modes (twist, vertical and horizontal) for fluidization of fine particles, Adv. Powder Technol. 12 (2001) 157-168. doi.org/10.1163/15685520052384998.

[29] D. Gidaspow, Multiphase Flow and Fluidization: Continuum and Kinetic Theory Descriptions, Elsevier Science1994.

[30] K. Niyogi, M.M. Torregrosa, M.N. Pantzali, G.J. Heynderickx, G.B. Marin, Experimentally validated numerical study of gas-solid vortex unit hydrodynamics, Powder Technol. 305 (2017) 794-808. doi.org/10.1016/j.powtec.2016.10.049.

[31] A. de Broqueville, J. De Wilde, Numerical investigation of gas-solid heat transfer in rotating fluidized beds in a static geometry, Chem. Eng. Sci. 64 (2009) 1232-1248. doi.org/10.1016/j.ces.2008.11.009.

[32] H.P. Zhu, Z.Y. Zhou, R.Y. Yang, A.B. Yu, Discrete particle simulation of particulate systems: A review of major applications and findings, Chem. Eng. Sci. 63 (2008) 5728-5770. doi.org/10.1016/j.ces.2008.08.006.

[33] H.P. Zhu, Z.Y. Zhou, R.Y. Yang, A.B. Yu, Discrete particle simulation of particulate systems: Theoretical developments, Chem. Eng. Sci. 62 (2007) 3378-3396. doi.org/10.1016/j.ces.2006.12.089.

[34] S. Golshan, R. Sotudeh-Gharebagh, R. Zarghami, N. Mostoufi, B. Blais, J.A.M. Kuipers, Review and implementation of CFD-DEM applied to chemical process systems, Chem. Eng. Sci. 221 (2020) 115646. doi.org/10.1016/j.ces.2020.115646.

[35] V. Verma, T. Li, J. De Wilde, Coarse-grained discrete particle simulations of particle segregation in rotating fluidized beds in vortex chambers, Powder Technol. 318 (2017) 282-292. doi.org/10.1016/j.powtec.2017.05.037.

[36] L. Lu, K. Yoo, S. Benyahia, Coarse-Grained-Particle Method for Simulation of Liquid–Solids Reacting Flows, Ind. Eng. Chem. Res. 55 (2016) 10477-10491. doi.org/10.1021/acs.iecr.6b02688.

[37] M. Sakai, M. Abe, Y. Shigeto, S. Mizutani, H. Takahashi, A. Viré, J.R. Percival, J. Xiang, C.C. Pain, Verification and validation of a coarse grain model of the DEM in a bubbling fluidized bed, Chem. Eng. J. 244 (2014) 33-43. doi.org/10.1016/j.cej.2014.01.029.

[38] J. De Wilde, G. Richards, S. Benyahia, Qualitative numerical study of simultaneous high-G-intensified gas–solids contact, separation and segregation in a bi-disperse rotating fluidized bed in a vortex chamber, Adv. Powder Technol. 27 (2016) 1453-1463. doi.org/10.1016/j.apt.2016.05.005.

[39] A. Gonzalez-Quiroga, S.R. Kulkarni, L. Vandewalle, P. Perreault, C. Goel, G.J. Heynderickx, K.M. Van Geem, G.B. Marin, Azimuthal and radial flow patterns of 1g-Geldart B-type particles in a gas-solid vortex reactor, Powder Technol. 354 (2019) 410-422. doi.org/10.1016/j.powtec.2019.06.015.

[40] C. Goniva, C. Kloss, N.G. Deen, J.A.M. Kuipers, S. Pirker, Influence of rolling friction on single spout fluidized bed simulation, Particuology 10 (2012) 582-591. doi.org/10.1016/j.partic.2012.05.002.

[41] OpenFOAM-v8, OpenFOAM Found. Ltd., openfoam.org (2021)

[42] C. Kloss, C. Goniva, A. Hager, S. Amberger, S. Pirker, Models, algorithms and validation for opensource DEM and CFD–DEM, Prog. Comput. Fluid Dyn. 12 (2012) 140-152. 10.1504/PCFD.2012.047457.

[43] Z.Y. Zhou, S.B. Kuang, K.W. Chu, A.B. Yu, Discrete particle simulation of particle–fluid flow: model formulations and their applicability, J. Fluid Mech. 661 (2010) 482-510. 10.1017/S002211201000306X.

[44] F.R. Menter, Two-Equation Eddy-Viscosity Turbulence Models for Engineering Applications, AIAA J. 32 (1994) 1598-1605. doi.org/10.2514/3.12149.

[45] B. Andersson, R. Andersson, L. Håkansson, M. Mortensen, R. Sudiyo, B. van Wachem, Computational Fluid Dynamics for Engineers, Cambridge University Press, Cambridge, 2011.

[46] D.J. Van Cauwenberge, C.M. Schietekat, J. Floré, K.M. Van Geem, G.B. Marin, CFD-based design of 3D pyrolysis reactors: RANS vs. LES, Chem. Eng. J. 282 (2015) 66-76. doi.org/10.1016/j.cej.2015.03.020.

[47] S. Ergun, Fluid flow through packed columns, 1952.

[48] C.Y.Y. Wen, Y.H., Mechanics of Fluidization, Chem. Eng. Prog. Symp. Ser. 162 (1966) 100-111

[49] H. Hertz, Ueber die Berührung fester elastischer Körper, J. für die Reine und Angew. Math. 92 (1882) 156-171. doi.org/10.1515/crll.1882.92.156.

[50] A. Gonzalez-Quiroga, P.A. Reyniers, S.R. Kulkarni, M.M. Torregrosa, P. Perreault, G.J. Heynderickx, K.M. Van Geem, G.B. Marin, Design and cold flow testing of a Gas-Solid Vortex Reactor demonstration unit for biomass fast pyrolysis, Chem. Eng. J. 329 (2017) 198-210. doi.org/10.1016/j.cej.2017.06.003.

[51] Pointwise, Pointwise Inc., Fort Worth, TX, 2015, pp. Mesh and grid generation software.

[52] R.I. Issa, Solution of the implicitly discretised fluid flow equations by operator-splitting, J. Comput. Phys. 62 (1986) 40-65. doi.org/10.1016/0021-9991(86)90099-9.

[53] https://www.engineeringtoolbox.com/friction-coefficients-d_778.html

[54] S. Bławucki, K. Zaleski, The effect of the aluminium alloy surface rougness on the restitution coefficient, Adv. Sci. Technol. Res. J. 9 (2015) 66-71. doi.org/10.12913/22998624/59086.

[55] G. Constantinides, C.A. Tweedie, N. Savva, J.F. Smith, K.J. Van Vliet, Quantitative Impact Testing of Energy Dissipation at Surfaces, Exp. Mech. 49 (2009) 511-522. doi.org/10.1007/s11340-008-9198-1.

[56] R. Seifried, H. Minamoto, P. Eberhard, Viscoplastic Effects Occurring in Impacts of Aluminum and Steel Bodies and Their Influence on the Coefficient of Restitution, J. Appl. Mech. 77 (2010). doi.org/10.1115/1.4000912.